RSC Advances

PAPER

View Article Online
View Journal | View Issue

Cite this: *RSC Adv.*, 2026, **16**, 24418

Effects of aromatic salts on the phase behavior and viscoelastic properties of a cationic gemini surfactant in aqueous solutions

Chenyu Zhao,[a] Song Lu,[a] Shuqi Cao,[b] Zhenghao Wu,[b] Linhua Wang,[b] Xuan Tang,[b] Bin Liu,[b] Meihua Gao*[c] and Huifang Xu *[a]

Received 25th February 2026
Accepted 27th April 2026

DOI: 10.1039/d6ra01652a

rsc.li/rsc-advances

Gemini surfactants, composed of two linked surfactant monomers, are capable of forming viscoelastic fluids in aqueous solution even at low concentrations. In this paper, two types of additives, benzoate and cinnamate derivatives, were introduced into aqueous solutions of the gemini surfactant 2-hydroxyltrimethylene-1,3-bis(tetradecyldimethylammonium chloride) (G_{14}) at varying molar ratios. The phase behavior, viscoelastic properties, and morphological transitions of the resulting systems were systematically investigated using rheology, dynamic light scattering, and cryogenic/negative-staining transmission electron microscopy. We demonstrate that structural features of the aromatic hydrotropes, such as hydroxyl, methyl, or methoxy substitutions and positional isomerism, critically regulate micellar growth and network entanglement. With increasing the hydrotrope-to-G_{14} molar ratio (R), the morphology transitions successively from spherical micelles to wormlike micelles and finally to vesicles. At an optimal R value of approximately 0.5, synergistic interactions between G_{14} and the hydrotrope promote maximal micellar elongation, yielding a highly entangled network and a corresponding maximum increase in zero-shear viscosity. The viscosity enhancement arises from the combined effects of electrostatic interactions, hydrogen bonding, and steric hindrance. This work establishes substituent-dependent structure–activity relationships for aromatic hydrotropes in gemini surfactant systems and provides a rational design strategy for tailoring wormlike micellar networks with potential applications in oil recovery, drug delivery, and specialized formulations.

1. Introduction

The ability to form hierarchically ordered aggregates, ranging from spherical and wormlike micelles to vesicles and lamellar structures, represents an intrinsic property of surfactants[1–3] or amphiphilic nanoparticles[4–6] in bulk solutions. This structural polymorphism further imparts multifunctional capabilities, making such systems suitable as drug delivery vehicles, solubilizing agents, and templates for nanomaterial synthesis.[7–10]

Cationic gemini surfactants, which consist of twin hydrophobic tails and hydrophilic head groups linked by a spacer near the polar region, exhibit superior aggregation properties compared to monomeric counterparts.[11,12] Their ability to form wormlike micelles (WLMs) at low concentrations without additives holds considerable industrial promise. However, the high cost of mass production limits the economic feasibility of single surfactant systems for large scale applications. This synergistic approach, which blends high-performance surfactants with cost-effective additives (*e.g.*, inorganic or organic salts) at optimized ratios, achieves comparable performance while improving both surface and bulk properties.[13–15] This makes the widespread industrial utilization of surfactant/counterion systems possible. A representative example is the cationic surfactant/aromatic salt system, which functions as a form of "molecular Lego": through precise modulation of weak interactions, including electrostatic, hydrophobic, and steric effects, it bridges nanoscale structural design with macroscopic performance optimization, thereby providing fundamental support for material innovation, biotechnology, and energy development.[16–18]

It is well known that aromatic salts can effectively screen the electrostatic repulsion among the charged headgroups of surfactants, thereby facilitating micellar elongation and the formation of wormlike micellar structures. Commonly employed aromatic additives, including salicylate, tosylate, and hydroxynaphthalenecarboxylate are frequently introduced into aqueous solutions of quaternary ammonium cations such as cetyltrimethylammonium halides and *N*-cetyl-

[a]College of Pharmacy, Henan University of Chinese Medicine, Zhengzhou 450046, P. R. China. E-mail: hfxu@hactcm.edu.cn
[b]School of Chemistry and Chemical Engineering, Liaocheng University, Liaocheng 252059, P. R. China
[c]School of Materials and Chemical Engineering, Xuzhou University of Technology, Xuzhou 221018, P. R. China. E-mail: mhgao@xzit.edu.cn

N-methylmorpholinium bromide or related derivatives to promote the development of viscoelastic wormlike micellar networks.[19–24] Although some literature has revealed that the aggregation behavior of the cationic surfactant micellar aqueous solutions was very sensitive to the presence of counterions, the specific influence of aromatic cosolutes on interfacial molecular packing and resulting macroscopic viscosity remains inadequately understood.[15,25] This lack of systemic research, in turn, significantly limits the broader application of these systems across various industrial fields. Subtle modifications in counterion structure and concentration can profoundly affect micellar contour length and flexibility, leading to significant changes in rheological properties. Such effects are closely linked to the extent and manner of counterion incorporation within the micellar assembly.[26,27]

In this paper, we systemically investigate the role of benzoate and cinnamate derivatives (13 aromatic salts, Fig. 1) in modulating the self-assembly and viscoelasticity of the cationic gemini surfactant (2-hydroxyltrimethylene-1,3-bis(tetradecyldimethylammonium chloride)) (G_{14}, Fig. 2). By combining rheometry, cryogenic/negative-staining transmission electron microscopy, and dynamic light scattering technique, we elucidate how structural modifications of these additives, including ring substitutions (hydroxyl, methyl, methoxy), substituent position, and electronic properties, govern the morphological evolution and viscoelastic response as a function of the molar ratio ($R = C_{\text{additives}}/C_{G_{14}}$). Our results reveal that the molar ratio critically dictates supramolecular morphological transitions, driven by competitive molecular interactions. Furthermore, the specific interplay between the organic salts and the gemini surfactant enables a reversible viscoelastic response, offering fundamental insights for the rational design of stimuli-responsive viscoelastic systems.

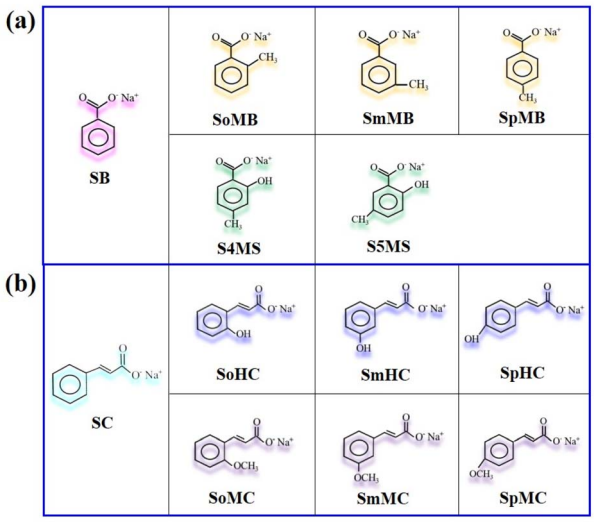

Fig. 1 Molecular structures of various aromatic additives: (a) sodium benzoate and its derivatives, (b) sodium cinnamate and its derivatives.

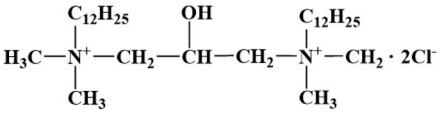

Fig. 2 Molecular structure of the gemini surfactant G_{14}.

2. Materials and methods

2.1. Materials

The cationic gemini surfactant G_{14} (or 14-3(OH)-14(2Cl), Fig. 2) was synthesized according to the methods reported in the literature.[28] The aromatic additives (Fig. 1), including sodium benzoate (SB, 99.5%), sodium *o*-hydroxybenzoate (SoHB, 99%), sodium *m*-hydroxybenzoate (SmHB, 99%), sodium *p*-hydroxybenzoate (SpHB, 99%), sodium *o*-methylbenzoate (SoMB, 99%), sodium *m*-methylbenzoate (SmMB, 99%), sodium *p*-methylbenzoate (SpMB, 98%), sodium 4-methylsalicylate (S4MS) and sodium 5-methylsalicylate (S5MS) with purity 99%, sodium cinnamate (SC, 99%), 2-hydroxycinnamic acid (SoHC, 98%), sodium 3-hydroxycinnamate (SmHC, 98%), sodium 4-hydroxycinnamate (SpHC, 99%), sodium *o*-methoxycinnamate (SoMC, 99%), sodium *m*-methoxycinnamate (SmMC, 99%) and sodium *p*-methoxycinnamate (SpMC, 98%) were obtained from Shanghai Chemical Co. Ltd and Sigma-Aldrich Reagent Co. China. Ultrapure water with a resistivity of 18.25 MΩ cm was obtained using a UPR-II-20T purification system (Sichuan ULUPURE Ultrapure Technology Co., Chengdu, China).

2.2. Sample preparation

A series of sample solutions with varying molar ratios between additives and G_{14} were prepared by mixing a fixed concentration (C) of G_{14} (80 mM) and varying concentrations of aromatic additives at equal volumes (1.5 mL) and swirled magnetically. The prepared solutions were maintained at 25 °C for at least 5 days to achieve equilibrium.

2.3. Rheological measurements

The rheological measurements were performed using an MCR 302 rheometer (Anton Paar, Austria) with either a parallel-plate (PP25, 25 mm diameter) or cone-plate geometry (CP25, 25 mm diameter), depending on the sample viscosity. A centrifuge was used to expel air bubbles in the samples before the measurements. The gap value between rotor and Peltier was 0.5 mm. The rheometer was installed with a Peltier plate, which can insure the precise control of the temperature (25 ± 0.05 °C). The dynamic sweeps were achieved at a fixed stress (selected in the linear range). All operations were repeated three times to ensure reproducibility.

2.4. Cryogenic transmission electron microscopy (Cryo-TEM)

The specimens for the Cryo-TEM measurement were prepared in a controlled environment vitrification system. A 5 μL aliquot of the sample solution was deposited onto a carbon-coated 300-

mesh copper grid. The grid was then blotted with filter paper for about 4 s to remove excess liquid and generate a thin film. About 10 s later, the grid was immediately plunged into liquid ethane and cooled to approximately −165 °C for vitrification. The vitrified grid was transferred under liquid nitrogen into a cryo-holder (Gatan 626) and observed at 120 kV using a JEM-1400 TEM equipped with a Gatan US1000 894 CCD camera.

2.5. Negative-staining transmission electron microscopy (NS-TEM)

Transmission electron microscopy (TEM) images of the samples were obtained using a JEM-2100 TEM instrument (JEOL, Japan), which was operated at an accelerating voltage of 200 kV. A volume of 10 μL of the sample solution was placed onto a 300-mesh copper grid coated with carbon, which was positioned on a piece of filter paper. Subsequently, 5 μL of a 1.5% (w/v) uranyl acetate solution was used for staining. Prior to observation, the specimens were stored in a desiccator for an entire night.

2.6. Dynamic light scattering (DLS)

DLS measurements were performed on a NanoBrook 90Plus PALS light scattering device (Brookhaven, USA) equipped with a 40 mW crystal laser to describe the size distribution and the average hydrodynamic diameter (D_h) of the aggregates. All the measurements were executed at a scattering angle of 90°, and the data were analyzed by means of the CONTIN method.[29]

3. Results and discussion

3.1. Phase behavior and steady-state rheology at variable additive ratios

The phase states of G_{14} solutions with a series of additives were observed by visual inspection (Fig. S1, SI). Before mixing, both the G_{14} solution and additive solution were transparent and non-viscous. This is consistent with previous literature, in which spherical and elliptical micelles coexist in the G_{14} solution in the absence of an added salt.[30] After mixing, the solutions in the tilted vials exhibited different states; variations in their flow behavior served as an indicator of differing viscoelasticity. The type and position of substituents exhibited significant differences in their capacity to enhance the viscosity of cationic surfactant systems. Upon tilting the vials (Fig. S2), the flow characteristics of these mixtures displayed varying gravitational responses. As the molar ratio R between the aromatic salt and surfactant ($R = C_{additives}/C_{G_{14}}$) increased, the mixed samples of all systems transitioned macroscopically from a fluid state to a gel-like state and then back to a fluid state. The viscosity of all systems initially increased and subsequently decreased with R increasing, with a peak at approximately 0.5.

It's worth noting that, with an increase in R, the systems exhibit a homogeneous transparent single-phase, a slightly bluish single-phase, and turbid dispersion with precipitates in turn, suggesting the structural transformation of aggregates in solutions (Fig. S2). This optical shift from a transparent phase to a bluish phase may arise from a morphological transition from worm-like micelles to vesicles or lamellar structures,[30] which will be verified by microscopic observation below.

Fig. 3 presents the steady-state rheological results for the G_{14}/SoMB, G_{14}/SmMB and G_{14}/SpMB systems. The 40 mM G_{14} aqueous solution (Fig. 3a, no additive) demonstrates near-constant apparent viscosity across the tested shear range ($\dot{\gamma}$), characteristic of Newtonian behavior. The ultralow zero-shear viscosity (η_0 = 0.00285 Pa s) further suggests the predominance of spherical or short ellipsoidal micellar assemblies. In contrast, all mixed systems exhibit distinct non-Newtonian characteristics: their steady-state viscosity curves establish a Newtonian plateau at low $\dot{\gamma}$, transitioning to pronounced shear-thinning above critical $\dot{\gamma}$. The observed shear-thinning behavior arises from two main mechanisms: the disruption of wormlike or rod-like micelles into smaller aggregates and the flow-induced alignment of micelles, both of which contribute to viscosity reduction.[31] The zero-shear viscosity (η_0) values of the mixed solutions for most systems were determined *via* extrapolation to $\dot{\gamma} \rightarrow 0$ using Carreau models.[32] For specific datasets exhibiting a sudden loss of data points at higher shear rates, the η_0 values were extracted directly from the experimental low-shear plateau due to the deviation of model fitting.

The η_0 value of the mixed solution initially remains constant as R increases (Fig. 4). However, when R exceeds a threshold value ($C_{additive} = C_S^*$, ~0.5), the η_0 begins to rise sharply probably due to the transformation of spherical micelles into wormlike micelles resulting from the uniaxial growth of the micelles. After reaching its maximum value, the viscosity abruptly drops and eventually stabilizes at a constant level. As shown in Fig. 4a, for the SoMB, SmMB and SpMB case, the maximum η_0 occurs at R = 0.65, 0.55, and 0.55, respectively. At a fixed ratio of 0.55, η_0 followed the order: SmMB > SpMB > SoMB. For the S4MS and S5MS case, η_0 reached a maximum at R = 0.4, with η_0 ranking as S4MS > S5MS (Fig. 4b). For the mixtures of G_{14} and sodium cinnamate or their derivates (Fig. 4c and d), the η_0 in most cases

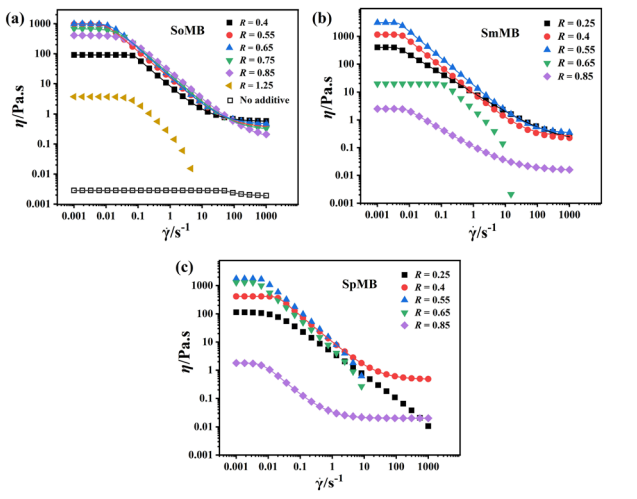

Fig. 3 Curves of viscosity (η) *versus* shear rate ($\dot{\gamma}$) for (a) G_{14}/SoMB, (b) G_{14}/SmMB and (c) G_{14}/SpMB systems as a function of R at 25 °C. The solid lines represent the fitted Carreau curves superimposed on the raw data (with R^2 value close to 1).

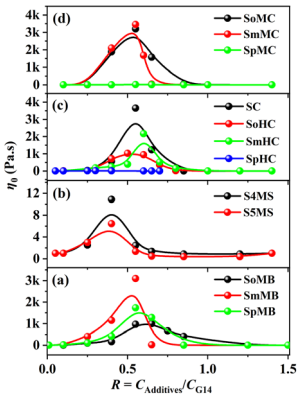

Fig. 4 Variation of zero-shear viscosity (η_0) for the G_{14} solutions in the presence of (a and b) benzoate derivatives and (c and d) cinnamate derivatives as a function of R at 25 °C.

initially increased and then decreased with a maximum at $R \sim 0.5$, similar to the mixtures of G_{14} and sodium benzoate or their derivates. In contrast, the G_{14}/SpHC and G_{14}/SpMC system exhibited consistently low viscosity, resulting in a plateau in η_0.

As stated above, the zero-shear viscosity of the mixed system reaches its maximum when the molar ratio R approaches 0.5. This suggests that stoichiometric interactions between the two components (*e.g.*, charge neutralization, hydrophobic matching, and hydrogen bonding) are most efficient at this ratio, maximizing micellar entanglement and network integrity. This phenomenon exhibiting the maximum viscosity followed by a decrease with increasing R is a typical behavior observed in numerous complex fluid systems containing cationic amphiphiles and hydrotropic co-solutes.[30,33,34] The decline in η_0 is frequently explained through two mechanistic perspectives: either the formation of branched wormlike micelles prompted by augmented end-cap energy[35,36] or alternatively, dimensional reduction of micellar assemblies resulting from constrained growth conditions.[37]

To evaluate how different isomeric additive influence intermolecular interactions with G_{14}, the molar ratio was held constant at $R = 0.4$ for all systems. Fig. 5 shows the visual appearance of the resulting mixtures. Their viscoelastic behavior was assessed qualitatively by tilting the vials and comparing flow resistance variations. In such systems, aromatic anions enhance viscoelasticity mainly through the electrostatic and hydrophobic modulation, and specific hydrogen bonding, which facilitates the formation of an entangled wormlike micellar network, yielding the pronounced viscoelasticity observed.

At $R = 0.4$, the apparent viscosity (η) *versus* shear rate curves for G_{14} solutions containing different benzoate and cinnamate derivatives were shown in Fig. 6. The η_0 value of each system, obtained by extrapolating to $\dot{\gamma} \rightarrow 0$ using Carreau models, is summarized in Table 1. For methybenzoate derivatives, η_0 follows the order: *meta*-substitution (SmMB) > *para*-substitution (SpMB) > *ortho*-substitution (SoMB). Notably, the *meta*-methylbenzoate system exhibits remarkable micellar elongation, yielding $\eta_0 = 1610$ Pa s, five orders of magnitude higher than that of the pure G_{14} solution (0.00285 Pa s), consistent with the formation of a persistent wormlike micellar networks. In contrast, orth-substituted analogues show substantially reduced viscoelasticity ($\eta_0 = 159$ Pa s for SoMB), indicating limited micellar growth. Sodium benzoate (SB) promotes intermediate network enhancement, exceeding SoMB but remaining below SmMB and SpMB.

The observed viscosity trend reflects differential penetration of aromatic counterions into the micellar palisade layer, with η_0 correlating directly with surfactant–counterion binding efficiency. Similar behavior has been documented in CTAB systems with hydroxybenzoates[38] and supported by microcalorimetric studies on alkyltrimethylammonium/isomer mixtures.[39] Notably, dual substitution introduces non-additive effects: coexisting hydroxyl and methyl groups on the benzoate ring (S4MS/S5MS) lower η_0 compared to their singly substituted counterparts, although S4MS retains relatively higher viscosity. This suggests competitive steric and electronic modulation of counterion binding, a phenomenon previously noted with multifunctional aromatic additives.[30] These results underscore that both substitution position and functional group multiplicity critically regulate counterion incorporation and packing, thereby governing micellar growth and network viscoelasticity.

3.2. Dynamic viscoelasticity of mixed solutions

The dynamic viscoelastic properties of mixed systems were characterized *via* oscillatory frequency sweeps under a constant

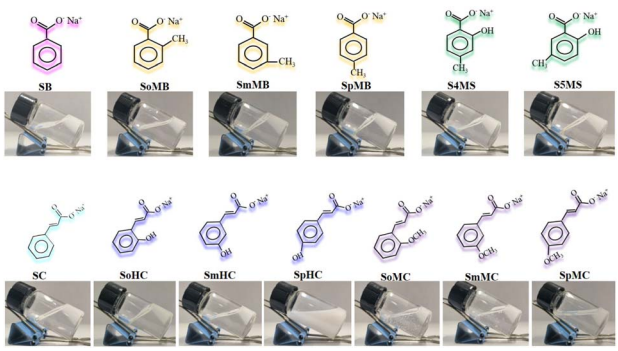

Fig. 5 Macroscopic appearance of the mixture solutions of G_{14} and various aromatic salts at $R = 0.4$.

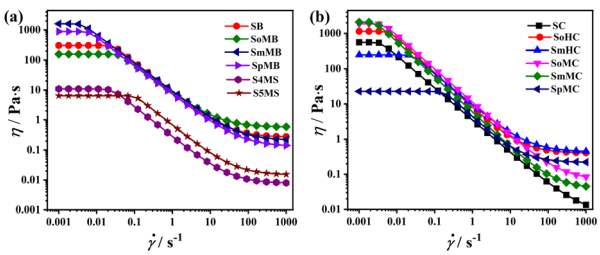

Fig. 6 Curves of apparent viscosity (η) *versus* shear rate ($\dot{\gamma}$) for the G_{14} solutions in the presence of (a) benzoate derivatives and (b) cinnamate derivatives at $R = 0.4$.

Table 1 Rheological parameters of wormlike micelles with various benzoate and cinnamate derivatives at $R = 0.4$

Hydrotropes	η_0/Pa s	ω_c/red s^{-1}	τ_R/s	G_0/Pa	G''_{min}/Pa	L_c/nm
G14	0.002850	3.027	0.3304	0.005090	0.02906	14.01–26.27
SB	301.0	0.02036	49.12	5.774	2.260	204.3–383.1
SoMB	159.0	0.06895	14.50	2.832	2.728	83.08–155.8
SmMB	1610	0.01574	63.53	7.068	1.171	482.8–905.3
SpMB	883.0	0.01593	62.77	6.313	1.258	401.5–752.8
S4MS	10.88	1.291	0.7750	2.763	6.583	33.58–62.96
S5MS	6.444	1.616	0.6188	2.261	5.453	33.17–62.20
SC	557.0	0.01641	60.94	5.962	1.562	305.4–572.6
SoHC	1150	0.01584	63.13	6.535	1.219	429.0–804.4
SmHC	250.0	0.06793	14.72	3.327	2.069	128.6–241.2
SoMC	1870	0.01539	64.98	8.080	1.233	524.1–982.7
SmMC	2100	0.01507	66.36	12.30	1.165	845.0–1584

shear stress ($\sigma = 0.1$ Pa). The pure G_{14} solution exhibited negligible storage modulus (G'), consistent with Newtonian behavior. Fig. 7 presents the angular frequency (ω) dependence of the storage (G') and loss (G'') moduli for representative systems for representative G_{14} systems containing sodium benzoate derivatives (Fig. 7a) and sodium cinnamate derivatives (Fig. 7b).

Except for the G_{14}/SpMC system, whose G' and G'' curves of the system did not intersect within the measured frequency range – indicating the presence of short, non-entangled micelle – all other mixed solutions displayed viscoelastic signatures characteristic of entangled wormlike micellar networks. These systems showed liquid-like behavior ($G'' > G'$), with a crossover to solid-like response ($G' > G''$) above a critical frequency ω_c (where $G' = G''$). The frequency-dependent viscoelasticity of such wormlike micellar solutions can be described by the Maxwell model:[40,41]

$$G' = \frac{(\omega\tau_R)^2}{1+(\omega\tau_R)^2}G_0 \quad (1)$$

$$G'' = \frac{(\omega\tau_R)}{1+(\omega\tau_R)^2}G_0 \quad (2)$$

where G_0 is the platform modulus and τ_R is the relaxation time, obtained as $\tau_R = 1/\omega_c$. A Cole–Cole plot (G'' *versus* G') was used to assess the fit to the Maxwell model, which ideally yields a semicircle:

$$G'' + \left(G' - \frac{G_0}{2}\right)^2 = \left(\frac{G_0}{2}\right)^2 \quad (3)$$

Kern *et al.*[42,43] recommended that G_0 could also be estimated *via* extrapolation from the Cole–Cole plot, where the data points deviating from the semicircle were projected onto the horizontal axis, yielding the plateau modulus G_0. When G_0 could not be directly determined, it was estimated from the viscous modulus (expressed as G''_{min}) at shear frequency ω_c, namely $G_0 = 2G''_{min}$.[44,45]

Key rheological parameters extracted from fitting the data in Fig. 6 and 7 are summarized in Table 1. The zero-shear viscosity (η_0) followed the order: SmMC > SoMC > SmMB > SoHC > SpMB > SC > SB > SmHC > SoMB > S4MS > S5MS > G_{14}, reflecting the overall viscosity strength of each system. Notably, the G_{14}/SpHC and G_{14}/SpMC mixtures appeared milky and formed precipitates upon standing (Fig. 5), indicating the formation of large aggregates or crystalline precipitates rather than a well-defined micellar network; thus, dynamic rheological data for these systems are not included. It can be seen that, both the relaxation time (τ_R) and plateau modulus (G_0) correlate with the contour length (L_c) of the wormlike micelles. Longer τ_R values signify micellar growth and enhanced entanglement, leading to higher viscosity, while G_0 relates to the density of entanglement strands and reflects the network mesh size. The relationship between G_0 and L_c for Maxwellian wormlike micelles is given by:

$$\frac{G_0}{G''_{min}} \approx \frac{L_c}{l_e} \quad (4)$$

where L_e (entanglement length) was taken as 80–150 nm based on previous work.[15]

Calculated L_c values ranged from 0.08–1.6 μm across different additive series, with methylcinnamates generally supporting the longest micelles. For the G_{14}/SB system, the L_c value was approximately 0.2–0.4 μm. In the G_{14}/methylbenzoate series, L_c varied from 0.08–0.9 μm depending on the methyl substitution site. Both G_{14}/S5MS and G_{14}/S4MS systems exhibited notably shorter L_c values, below 0.06 μm. For the G_{14}/

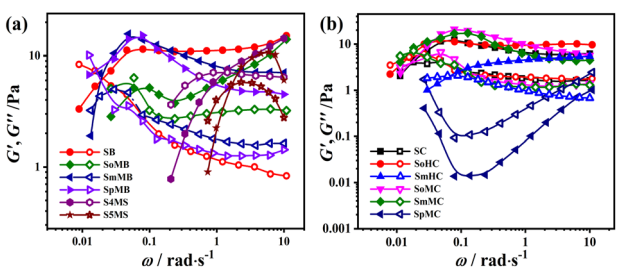

Fig. 7 Dynamic moduli as a function of oscillation frequency for the aqueous G_{14} solutions containing (a) sodium benzoate derivatives and (b) sodium cinnamate derivatives at $R = 0.4$ at 25 °C. The closed symbol and open symbol represent storage shear modulus G' and loss shear modulus G'', respectively.

hydroxycinnamate series, L_c spanned 0.1–0.8 μm with hydroxyl position variation, while in the G_{14}/methylcinnamate series, L_c extended from 0.5 to 1.6 μm as a function of methyl substitution.

Rheological analysis further reveals clear substituent-dependent trends in micellar growth. Among methylbenzoates, the promotion efficacy follows SmMB > SpMB > SoMB. In the hydroxycinnamate series, SoHC outperforms SmHC, whereas among methylcinnamates, SmHC leads, followed by SoHC. These growth tendencies align closely with the observed zero-shear viscosity (η_0) trends, confirming that longer micellar contour lengths correspond directly to enhanced network viscoelasticity. Overall, the results highlight that both the type and positional isomerism of the aromatic additive critically regulate micellar elongation, thereby governing the macroscopic rheological response of the mixed systems.

3.3. Cryo-TEM analysis and mechanistic insights into co-assembled micelles

As described previously, the mixed solutions underwent distinct phase transitions with increasing molar ratio R: from a transparent, low-viscosity single phase at low R, to a viscous, flow-resistant state, and finally to a bluish, turbid yet fluid phase when R exceeded approximately 0.5. This evolution corresponds to a progressive transformation of self-assembled structures from spherical micelles to wormlike micelles and eventually to vesicles.

To confirm this structural transition, the aggregates in the G_{14}/SmMC system were characterized using TEM and DLS. At R = 0.55, cryo-TEM imaging (Fig. 8a) confirmed the presence of wormlike micelles across mixtures. At R = 0.85, polydisperse vesicles with varied morphologies, including spherical, tubular, and bilayer structures, were observed (Fig. 8b). These vesicles exhibited relatively flexible membranes, with occasional negative curvature. Birefringence under crossed polarizers further supported the presence of bilayer assemblies. NS-TEM analysis corroborated these findings, revealing predominantly unilamellar vesicles along with a minority of multilamellar structures, as shown in (Fig. 8c and S3). DLS serves as a highly effective and compelling technique that macroscopically demonstrates changes in the dimensions of aggregate structures in solutions.[14,46,47] As shown in Fig. 9, with R increasing from 0 to 0.85, the aggregate size shifted from micellar dimensions (~10 nm) toward a broad distribution of vesicular structures ranging from 50 nm to 2 μm. Intensity- and volume-weighted profiles confirmed this polydispersity, while number-weighted distributions indicated that most vesicles were around 100 nm in diameter. The observed changes in macroscopic viscosity directly correlate with these structural transformations, as summarized schematically in Fig. 10a.

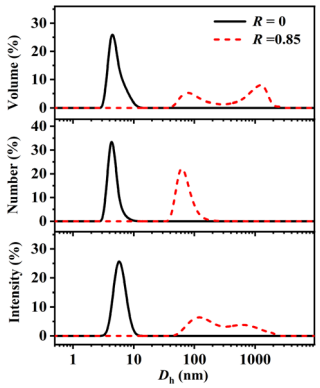

Fig. 9 Intensity-, number- and volume-weighted size distribution of the aggregates in the G_{14}/SpMC solutions at R = 0 and R = 0.85.

According to the molecular packing parameter framework proposed by Israelachvili *et al.*,[48] this structural evolution is governed by changes in the molecular packing parameter ($P = v/a_0 \cdot l_c$). The transition toward lower-curvature morphologies arises from two complementary intermolecular effects: electrostatic screening of the cationic headgroups by aromatic carboxylate anions, which reduces headgroup repulsion and decreases the effective cross-sectional area a_0; and hydrophobic insertion of the aromatic moieties into the micellar core, which increases the effective chain volume v. The concurrent decrease in a_0 and increase in v elevate P, thereby driving the progression from spherical micelles to wormlike micelles and eventually vesicles. Furthermore, hydrogen bonding between the hydroxyl groups of G_{14} and aromatic anions enhances intermolecular association, stabilizing the formed assemblies, while π–π stacking and hydrophobic interactions within the aromatic groups contribute to bilayer cohesion in vesicular structures.

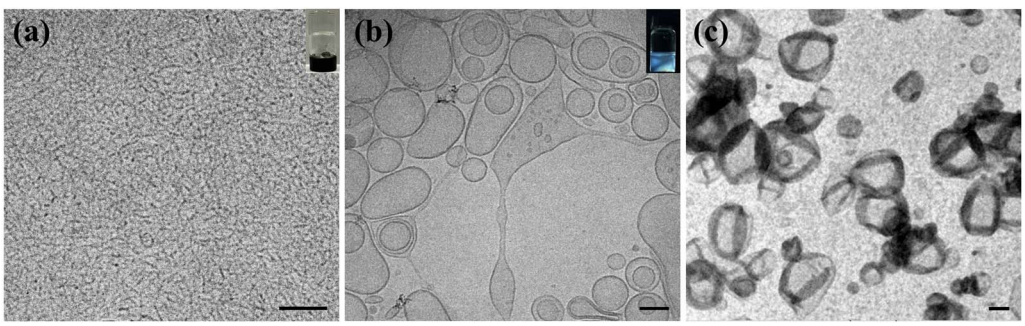

Fig. 8 Cryo-TEM (a and b) and NS-TEM (c) images of G_{14}/SmMC solutions at different R. (a) R = 0.55 and (b and c) R = 0.85. The insets are the optical photographs of sample solutions without (a) or with (b) crossed polarizers. Scale bar = 100 nm.

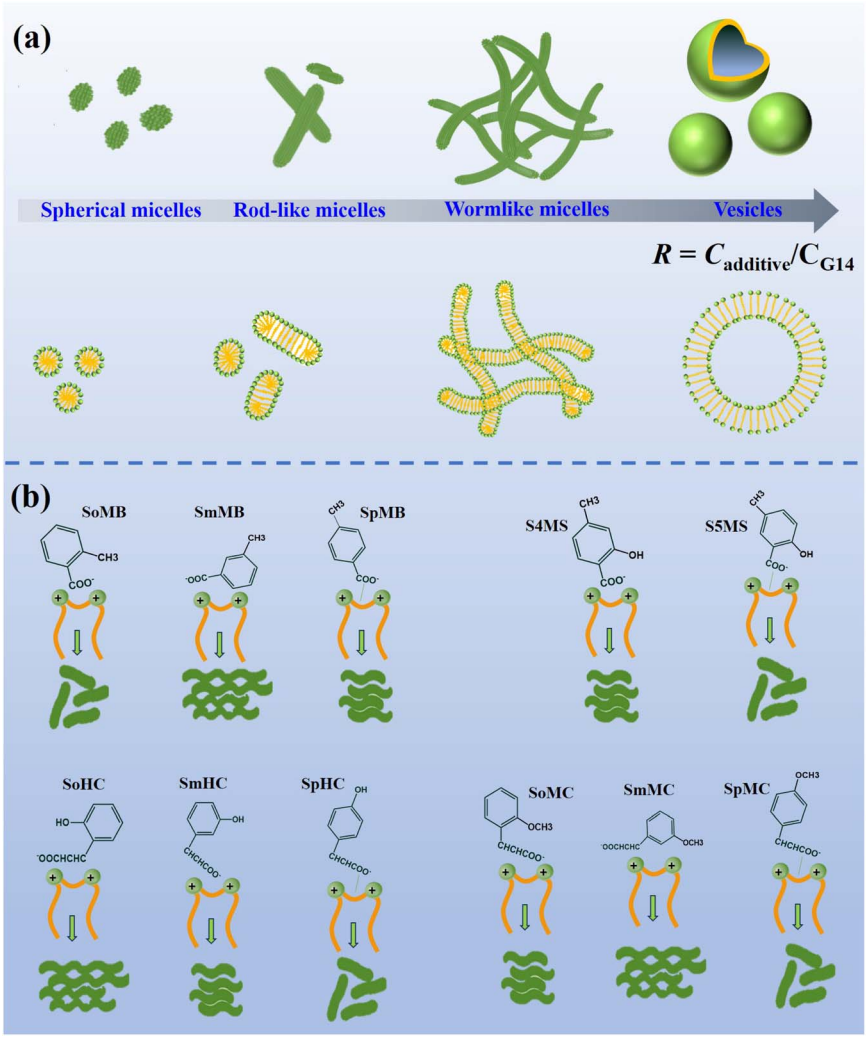

Fig. 10 (a) Schematic depiction of microstructural evolution with increasing R and (b) proposed mechanisms underlying the substituent-induced variation in rheological behavior of mixed micelle systems.

Compared with inorganic salts, whose effect is dominated by electrostatic screening, organic hydrotropes modulate micellar transitions through a more complex interplay of intermolecular forces, including electrostatic, hydrophobic, π–π stacking, and hydrogen-bonding interactions. Key factors governing these transitions include: (1) the positional isomerism of substituents (*ortho*, *meta*, *para*); (2) the competitive hydrophilic–lipophilic balance; (3) steric constraints on molecular packing; (4) directional hydrogen-bonding capacity; (5) electronic properties of the aromatic system; and (6) synergistic interplay among functional groups, such as co-localization of methyl and hydroxy moieties. Together, these factors critically influence micellar growth kinetics, persistence length, and entanglement density, thereby ultimately determining macroscopic rheological behavior.

To systematically illustrate how these molecular parameters govern micellar structure and rheology, we next examine isomer-specific effects at a fixed molar ratio of $R = 0.55$. At this ratio, the zero-shear viscosity (η_0) of methylbenzoate isomers follows the order: SmMB > SpMB > SoMB (Fig. 4). This trend cannot be fully explained by the effective surfactant headgroup area alone, which follows SoMB > SmMB > SpMB. This can be ascribed to the significantly larger steric hindrance of the methyl group in SoMB than that of SmMB. Specifically, the *ortho*-methyl group in SoMB imposes the largest steric barrier, preventing close molecular packing and leading to sharply reduced viscosity (Fig. 10b). However, the observed η_0 order is ultimately dictated by specific hydrogen-bonding interactions. The carboxylate of SmMB forms favorably oriented hydrogen bonds with the hydroxyl groups of the gemini surfactant G_{14}, promoting tight molecular packing and extensive micellar elongation, which yields the highest η_0. In contrast, SpMB forms relatively linear hydrogen bonds that appear to restrict micellar growth compared to the *meta*-isomer, while SoMB suffers from dominant *ortho*-methyl steric effects, resulting in loose complexes and the lowest viscosity. Therefore, despite a smaller headgroup area, SpMB exhibits lower η_0 than SmMB, establishing the final order: SmMB > SpMB > SoMB.

In hydroxybenzoate systems, the position of the methyl group further modulates hydrogen-bonding patterns. For S4MS (methyl at position 4), intramolecular hydrogen bonding dominates, weakening intermolecular interactions and reducing directionality. In contrast, S5MS (methyl at position 5) favors intermolecular hydrogen bonding, which promotes cross-linking and improves alignment between the carboxylate and the hydroxyl groups of G_{14}, thereby enhancing hydrogen-bond linearity (Fig. 10b).

Among hydroxycinnamates, η_0 follows SoHC > SmHC > SpHC at $R = 0.55$ (Fig. 4). SoHC adopts an upright orientation at the micellar interface, facilitating micellar growth and superior viscoelasticity. The carboxyl group of SmHC tilts relative to the interface, increasing steric bulk and restricting micellar elongation. SpHC forms linear hydrogen bonds that severely limit micellar growth, leading to the shortest micelles and the lowest viscosity (Fig. 10b).

For methoxycinnamate derivatives, η_0 at $R = 0.55$ decreases in the order SmMC > SoMC > SpMC at $R = 0.55$ (Fig. 4). Geometrically, the distance between the carboxylate and methoxy groups increases as SoMC < SmMC < SpMC, corresponding to effective headgroup areas of SoMC > SmMC > SpMC. Although *ortho*-methoxy substitution in SoMC imposes steric hindrance that hinders tight packing and reduces viscosity relative to SmMC, *para*-methoxy substitution in SpMC facilitates the formation of linear hydrogen bonds with G_{14} due to low steric hindrance and optimized molecular symmetry. These linear bonds severely restrict micellar growth, ultimately yielding the lowest η_0 despite SpMC having the smallest headgroup area (Fig. 10b).

In summary, the macroscopic viscoelastic behavior of these mixed systems arises from a delicate balance between steric constraints, which govern headgroup packing, and directional non-covalent interactions, particularly hydrogen bonding. Isomer-specific variations in molecular geometry and interaction patterns collectively determine the extent of micellar elongation and network entanglement, underpinning the distinct rheological profiles observed for each additive.

4. Conclusions

This study systematically explores the co-assembly of the gemini surfactant G_{14} with 13 structurally varied aromatic hydrotropes across a range of molar ratios. With increasing hydrotrope-to-G_{14} molar ratio, the aggregate structures in the mixed solutions progressively transition from initial spherical micelles to wormlike micelles, and finally form spherical vesicle structures. The viscoelastic response is strongly governed by the type and position of substituents on the aromatic counterions. In particular, the spatial separation between the carboxyl group and adjacent substituents (–OH, $–CH_3$, or $–OCH_3$) critically modulates the electrostatic screening and hydrogen-bond accessibility. *Ortho*-substituted hydroxybenzoate and cinnamate derivatives exhibit the highest binding affinity toward G_{14}, while *para*-substituted analogues show opposite interaction trends. Mechanistic insights, based on zero-shear viscosity measurements and intermolecular interaction evaluation, reveals that synergistic electrostatic attraction and directional hydrogen bonding reduce the interfacial curvature of micelles. This promotes uniaxial growth and the transition from spherical to elongated micellar morphologies, whose subsequent entanglement results in pronounced viscosity enhancement. These findings provide clear molecular guidelines for the rational design of stimuli-responsive wormlike micellar systems, with potential applications in areas such as drag reduction, controlled release, and functional soft materials.

While this study focuses on aromatic hydrotropes bearing electron-donating substituents, it is worth noting that aromatic salts with electron-withdrawing groups are also expected to promote wormlike micelle formation through similar mechanisms of electrostatic screening and hydrophobic penetration. The relative efficacy, however, may differ due to substituent effects on counterion binding affinity, hydration, and specific intermolecular interactions. A systematic comparison between electron-donating and electron-withdrawing substituted aromatic salts represents a promising direction for future investigation.

Conflicts of interest

There are no conflicts to declare.

Data availability

The data that support the findings of this study are included in this published article.

Supplementary information: the macroscopic appearance and TEM images for the mixed solutions. See DOI: https://doi.org/10.1039/d6ra01652a.

Acknowledgements

This work is supported financially by the National Natural Science Foundation of China (No. 22302165), Natural Science Foundation of Henan (No. 262300422421), Key Research & Development and Promotion Projects of Henan Province (No. 262102230115), and Liaocheng University Students Innovation and Entrepreneurship Training Program (No. CXCY2025051 and CXCY2025053) for financial support.

Notes and references

1 Y. Mai and A. Eisenberg, *Chem. Soc. Rev.*, 2012, **41**, 5969–5985.
2 T. Liu, P. Yi, Z. Xia, J. Dong and X. Li, *Acta Phys.-Chim. Sin.*, 2020, **36**, 1910004.
3 L. Su, J. Mosquera, M. F. J. Mabesoone, S. M. C. Schoenmakers, C. Muller, M. E. J. Vleugels, S. Dhiman, S. Wijker, A. R. A. Palmans and E. W. Meijer, *Science*, 2022, **377**, 213–218.
4 B. Liu, D.-M. Lv, Y.-L. Wang, W.-Y. Li, Y.-W. Sun and Z.-W. Li, *Langmuir*, 2024, **40**, 6363–6374.

5 U. K. Dey, S. Demirci, R. Ortega, T. Rawah, A. Chaudary, F. Liu, Z. Yang, B. Huang and S. Jiang, *Langmuir*, 2025, **41**, 2980–2993.
6 B. Liu, S. Yin, X. Wu, Z. Wu, D. Lv, Y. Wang and Z. Li, *Colloids Surf., A*, 2025, **719**, 136986.
7 L. L. Schramm, E. N. Stasiuk and D. G. Marangoni, *Annu. Rep. Prog. Chem., Sect. C: Phys. Chem.*, 2003, **99**, 43–48.
8 L. Gong, G. Liao, Q. Chen, H. Luan and Y. Feng, *Acta Phys.–Chim. Sin.*, 2019, **35**, 816–828.
9 Y. Liu, L. Wang, L. Zhao, Y. Zhang, Z.-T. Li and F. Huang, *Chem. Soc. Rev.*, 2024, **53**, 1592–1623.
10 K. L. A. Cao, D. B. Kautsar, K. Kume, K. A. L. Cao, E. L. Septiani, T. Hirano, N. Tsunoji, M. Matsukata and T. Ogi, *ACS Appl. Mater. Interfaces*, 2025, **17**, 24310–24326.
11 F. M. Menger and C. A. Littau, *J. Am. Chem. Soc.*, 1991, **113**, 1451–1452.
12 H. Dahal, A. M. Paswan, J. Dey and C. R. Raj, *Langmuir*, 2025, **41**, 5455–5466.
13 G. C. Maitland, *Curr. Opin. Colloid Interface Sci.*, 2000, **5**, 301–311.
14 B. Liu, M. Liu, Z. Wu, M. Zhang, F. Meng, Y. Wang, N. Du and H. Xu, *J. Mol. Liq.*, 2024, **410**, 125613.
15 B. Liu, S. Yin, X. Wu, X. Wei, H. Xu, J. Li and D. Lv, *Molecules*, 2024, **29**, 5482.
16 R. A. Gonçalves, K. Holmberg and B. Lindman, *J. Mol. Liq.*, 2006, **55**, 381–390.
17 Y. Zhong, Y. Xu, J. Ma, C. Wang, S. Sheng, C. Cheng, M. Li, L. Han, L. Zhou and Z. Cai, *Angew. Chem., Int. Ed.*, 2020, **132**, 19257–19263.
18 R. A. Gonçalves, K. Holmberg and B. Lindman, *J. Mol. Liq.*, 2023, **375**, 121335.
19 X. M. Pei, J. X. Zhao, Y. Z. Ye, Y. You and X. L. Wei, *Soft Matter*, 2011, **7**, 2953–2960.
20 T. S. Davies, A. M. Ketner and S. R. Raghavan, *J. Am. Chem. Soc.*, 2006, **128**, 6669–6675.
21 E. J. Creatto, F. B. Okasaki, M. B. Cardoso and E. Sabadini, *J. Colloid Interface Sci.*, 2022, **627**, 355–366.
22 Y. Tu, Q. Z. Chen, Y. Z. Shang, H. N. Teng and H. L. Liu, *Langmuir*, 2019, **35**, 4634–4645.
23 X. Q. Cao, W. L. Guo, Q. Zhu, H. J. Ge, H. Yang, Y. B. Ke, X. H. Shi, X. Y. Lu, Y. J. Feng and H. Y. Yin, *J. Colloid Interface Sci.*, 2023, **649**, 403–415.
24 G. C. Kalur, B. D. Frounfelker, B. H. Cipriano, A. I. Norman and S. R. Raghavan, *Langmuir*, 2005, **21**, 10998–11004.
25 W. X. Liu, Z. C. Ye, Q. Z. Chen, X. R. Huang, Y. Z. Shang, H. L. Liu, H. Meng, Y. F. He and Y. M. Dong, *Langmuir*, 2021, **37**, 9518–9531.
26 Y. Q. Nan, S. Wang and C. Yuan, *Colloids Surf., A*, 2026, **728**, 138767.
27 Z. L. Chu, C. A. Dreiss and Y. J. Feng, *Chem. Soc. Rev.*, 2013, **42**, 7174–7203.
28 Z. Wei, X. Wei, D. Sun, J. Liu and X. Tang, *J. Colloid Interface Sci.*, 2011, **354**, 677–685.
29 S. W. Provencher, *Comput. Phys. Commun.*, 1982, **27**, 229–242.
30 X.-X. Chen, Q. Liu, Y. Guo, H. Yan, J. Li, D.-M. Lv, J.-H. Zhang, M. Liu, C.-H. Yao and X.-L. Wei, *Soft Matter*, 2018, **14**, 6696–6707.
31 M. Johnsson, A. Wagenaar, M. C. A. Stuart and J. B. F. N. Engberts, *Langmuir*, 2003, **19**, 4609–4618.
32 P. J. Carreau, *Trans. Soc. Rheol.*, 1972, **16**, 99–127.
33 T. S. Davies, A. M. Ketner and S. R. Raghavan, *J. Am. Chem. Soc.*, 2006, **128**, 6669–6675.
34 Y. Lin, X. Cheng, Y. Qiao, C. Yu, Z. Li, Y. Yan and J. Huang, *Soft Matter*, 2010, **6**, 902–908.
35 M. In, G. G. Warr and R. Zana, *Phys. Rev. Lett.*, 1999, **83**, 2278–2281.
36 S. R. Raghavan and E. W. Kaler, *Langmuir*, 2001, **17**, 300–306.
37 L. Ziserman, L. Abezgauz, O. Ramon, S. R. Raghavan and D. Danino, *Langmuir*, 2009, **25**, 10483–10489.
38 R. G. Shrestha, K. Nomura, M. Yamamoto, Y. Yamawaki, Y. Tamura, K. Sakai, K. Sakamoto, H. Sakai and M. Abe, *Langmuir*, 2012, **28**, 15472–15481.
39 M. A. Rub, N. Azum, F. Khan and A. M. Asiri, *J. Phys. Org. Chem.*, 2017, **30**, 51–61.
40 M. E. Cates, *J. Phys.: Condens. Matter*, 1996, **8**, 9167–9176.
41 M. Kröger and J. Vermant, *Appl. Rheol.*, 2000, **10**, 110–111.
42 P. L. F. Kern, S. J. Candau and M. E. Cates, *Langmuir*, 1992, **8**, 431–440.
43 F. K. Lequeux, F. Zana, R. Candau and S. Jean, *Langmuir*, 1994, **10**, 1714–1723.
44 D. P. Acharya, K. Hattori, T. Sakai and H. Kunieda, *Langmuir*, 2003, **19**, 9173–9178.
45 D. P. Acharya, K. Hattori, S. Yositaka and K. Aratani, *J. Phys. Chem. B*, 2004, **108**, 1790–1797.
46 B. Liu, M. Gao, H. Li, J. Liu, S. Yuan, N. Du and W. Hou, *Phys. Chem. Chem. Phys.*, 2018, **20**, 1332–1336.
47 B. Liu, Y. Wang and N. Du, *Molecules*, 2023, **28**, 28093929.
48 J. N. Israelachvili, D. J. Mitchell and B. W. Ninham, *J. Chem. Soc., Faraday Trans.*, 1976, **72**, 1525–1568.